

Article

Electromagnetic Design and Analysis of Inertial Mass Linear Actuator for Active Vibration Isolation System

Do-Kwan Hong^{1,2,*}  and Jang-Hyun Park^{1,2}

¹ Electric Machine and Drive Research Center, Korea Electrotechnology Research Institute, Changwon 51543, Republic of Korea; jhpark7@keri.re.kr

² Electric Energy Conversion Engineering, University of Science and Technology, Changwon 51543, Republic of Korea

* Correspondence: dkhong@keri.re.kr; Tel.: +82-(0)10-9601-9234

Abstract: Underwater radiated noise from anthropogenic structures must be reduced to protect the marine environment. Active vibration isolation that can reduce noise generated from vibration sources by providing counteracting forces can solve this issue. This paper presents a 120 N class electromagnetic inertial mass linear actuator for an active vibration control system in a large ship. The proposed actuator is operated based on the Lorentz force, also known as electromagnetic force. To achieve a high thrust force to weight ratio, a permanent magnet with outer radial magnetization is used. In order to design and analyze the proposed model, a simple magnetic equivalent circuit analysis was first conducted to achieve an appropriate force, and its value was compared and verified with the magnetostatic finite element method. The dynamic characteristics of the actuator were then evaluated, and the performance was analyzed at various operating frequency points. The bobbin housing supporting the coil causes an eddy current loss due to materials with electrical conductivity. As a result, the damping force is generated by the reduction in magnetic flux, and the control force tends to decrease.

Keywords: active vibration isolation; inertial mass linear actuator; electromagnetic actuator; magnetic equivalent circuit; ship engine vibration and noise



Citation: Hong, D.-K.; Park, J.-H. Electromagnetic Design and Analysis of Inertial Mass Linear Actuator for Active Vibration Isolation System. *Actuators* **2023**, *12*, 295. <https://doi.org/10.3390/act12070295>

Academic Editor: Ioan Ursu

Received: 4 July 2023

Revised: 15 July 2023

Accepted: 18 July 2023

Published: 20 July 2023



Copyright: © 2023 by the authors. Licensee MDPI, Basel, Switzerland. This article is an open access article distributed under the terms and conditions of the Creative Commons Attribution (CC BY) license (<https://creativecommons.org/licenses/by/4.0/>).

1. Introduction

Underwater radiated noise (URN), which refers to the increase in ambient noise levels caused by large ships, is an important issue in the marine environment [1–3]. Prolonged exposure to high levels of URN can lead to significant impact on marine mammals. Moreover, high levels of URN during naval operations are easily detected by sonar. Some primary noise sources of a large ship are propellers with cavitation on the blade, the hull, generators, the engine, and auxiliary machinery and equipment. In particular, vibration and noise generated from an engine that requires a high-power output to rotate the propeller of a ship are considerable. Ships are commonly equipped with mechanical hydraulic systems as a steering gear to control propeller direction. Hydraulic systems also generate high vibration with low-frequency noise from pressure fluctuations [4]. The vibrations and noise from ships propagate through the ship's structure as structure-borne noise (SBN) and into the water as URN [3].

To minimize vibration and noise from an engine or machinery in maritime applications, vibration isolation systems have been widely used. Vibration isolation systems are broadly divided into passive vibration isolation (PVI) systems and active vibration isolation (AVI) systems [5]. PVI systems, such as a spring mount and rubber mount, are structurally simple and inexpensive, but provide vibration isolation for a limited frequency range only. PVI systems are operated by designing these passive control frequency ranges to be as close as possible to the vibration frequencies of machinery [6]. On the other hand, AVI systems with an actuator can address a wide range of vibration frequencies and amplitudes and

provide monitoring and diagnostics using real-time sensors to check whether there is a malfunction situation or not [7–9]. Although AVI systems offer significant advantages compared to PVI systems, they also have disadvantages, such as complex inner structures and control algorithms. Most maritime applications of vibration isolation systems consist of a hybrid isolation system combining PVI and AVI systems, as this offers advantages in terms of overcoming a complex structure and high cost [10–16]. In a hybrid isolation system, a PVI system is used to support heavy machinery, while an AVI system is used to attenuate the engine vibration. Furthermore, if the AVI system malfunctions, the PVI system can continually conduct vibration attenuation.

There are various types of actuators, such as piezoelectric actuators, hydraulic and pneumatic actuators, electromagnetic inertial mass actuators, etc. [17]. Piezoelectric actuators have the highest precision resolution but can easily break [17,18]. While hydraulic and pneumatic actuators can control large machinery, they require large equipment that is not applicable for limited spaces, such as on a large ship. In addition, they have low resolution and difficulty controlling high-frequency region. Although high-frequency vibrations can be control by using servo valves or proportional directional control valves, these need more complex and large volume.

Electromagnetic actuators, meanwhile, have relatively lower precision resolution than piezoelectric actuators. However, they offer greater strength to external shocks than piezoelectric actuators. Large ships or other marine applications can undergo rapid engine acceleration or unexpected external impulse loading by shock waves to the hull of a ship. Compared to hydraulic and pneumatic actuators, electromagnetic actuators can control the high-frequency region. Therefore, considering high strength with high precision resolution and the wide frequency control region, an electromagnetic actuator is selected for an AVI system for a large ship in this work. The concept of an AVI system with an electromagnetic actuator in a large ship is illustrated in Figure 1. The AVI system generates anti-phase counteracting dynamic forces to the engine vibration. The amplitude and frequency of external vibration detected by a real time sensor are transmitted to the controller and, based on this, the controller adjusts the frequency and current amplitude of the amplifier.

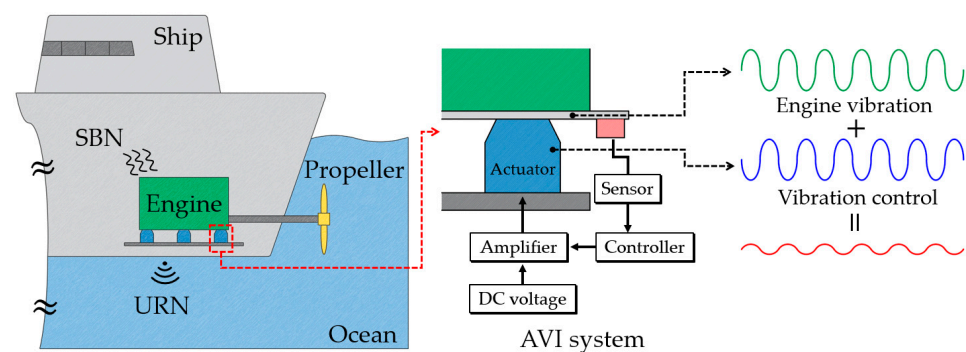


Figure 1. Conceptual illustration of active vibration isolation system in a ship.

Electromagnetic actuators based on the Lorentz force can be divided into moving voice coil actuators (VCMs) [19–21] and moving inertial mass actuators (IMAs) [22–24]. Structurally, the IMAs and VCAs are similar in appearance, as shown in Figure 2. However, the moving part of a VCA is the coil part, as shown in Figure 2a. On the other hand, the coil part of the IMA as shown in Figure 2b is fixed, and the solid core and PM are used as the moving part to generate inertial mass force. An IMA typically consists of a mass that is mechanically connected to a load and can be accelerated or decelerated to create a force. It can generate higher force compared to a VCA by using an inertial mass; an IMA is, thus, more suitable for applications that require high force.

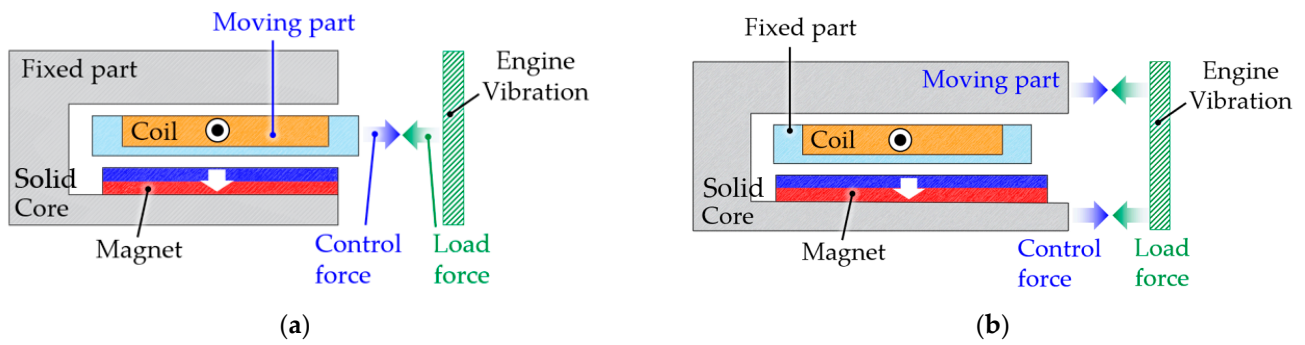


Figure 2. (a) Schematic diagram of VCA; (b) schematic diagram of IMLA.

This work mainly focuses on the electromagnetic design and analysis of an inertial mass linear actuator (IMLA) for an active vibration isolation system. First, the configuration and operation principle of the proposed IMLA are explained. Second, the generated Lorentz force of the proposed IMLA is predicted and analyzed by a simple magnetic equivalent circuit (MEC). The predicted Lorentz force is compared with the results of a finite element method (FEM). Finally, dynamic characteristics are evaluated for the eddy current damping effect in the bobbin housing, solid cores, and permanent magnet (PM). The results show that the damping effect of the bobbin is significant, which leads to a decrease in Lorentz force from the coil parts.

2. Proposed Inertial Mass Linear Actuator for Active Vibration Isolation Mount

The proposed IMLA, as shown in Figure 3a, has a cylindrical shape with winding (coil) with the bobbin housing, an outer radial magnetized PM, and a solid core. It must be designed within a constraint volume of $90 \times 90 \times 110 \text{ mm}^3$ (x - y - z axis direction as shown in Figure 3a, respectively). The proposed IMLA is concerned with a three-axis direction active vibration isolation system that utilizes three IMLAs, which means they are used as multiple vibration isolators. Here, the bobbin housing and winding are the fixed part, whereas the PM and solid core are the moving part. When Lorentz force is generated in the winding, the reaction force is transmitted to the moving part. The moving part is combined in parallel with a circular plate spring connected with the load part.

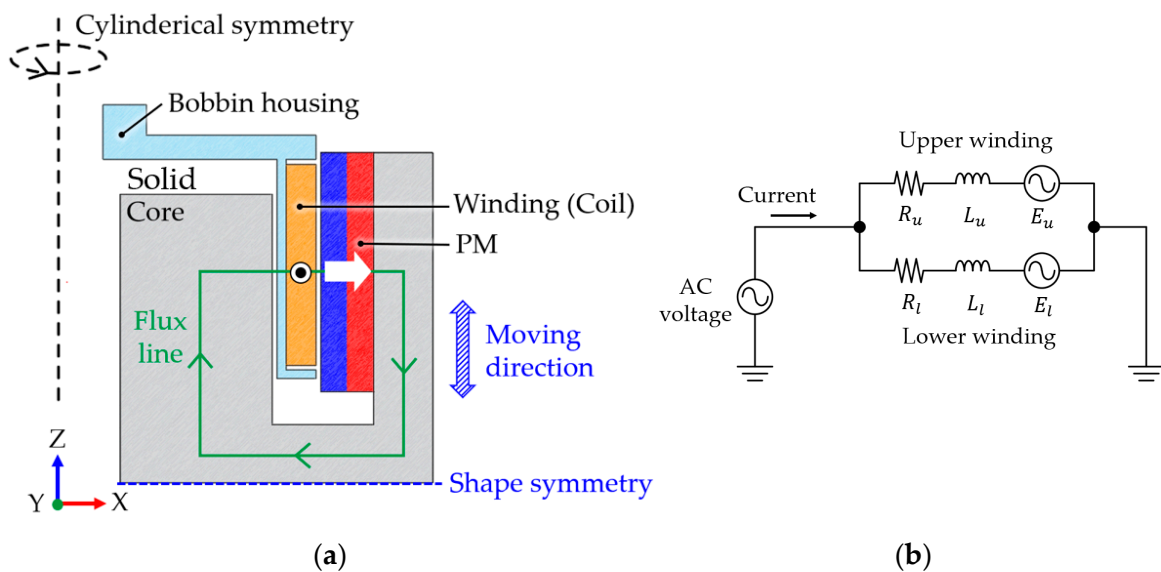


Figure 3. (a) Two-dimensional model of the proposed IMLA; (b) electric equivalent circuit of the proposed IMLA.

High inductance can cause a slow time constant, which can limit the overall performance. Thus, to reduce inductance, two parallel connections to the upper and lower parts, as illustrated in Figure 3b, are configured. Back-electromagnetic force (EMF) is induced in the winding when operating the moving part by changing the magnetic field of the PM.

Table 1 presents the required specifications for the proposed IMLA. Operation of precision control requires an operating force of at least 120 N at an operating frequency three times higher than the natural frequency f_n of the proposed IMLA. To achieve a high power per unit volume, neodymium, a PM material that has high residual flux density, was selected.

Table 1. The required specifications of the proposed ITPA.

	Items	Value	Remark
	The required load force (N)	120	Over $3f_n$
	Operating frequency (Hz)	$3f_n \sim 400$	
Materials	Solid core	Carbon steel (S20C)	
	Winding	Copper	
	PM	Neodymium N48 (80 °C)	
	Bobbin housing	Aluminum	

The force of the proposed IMLA is based on the Lorentz force $\vec{F}_L(t)$, which is defined as follows:

$$\begin{aligned}\vec{F}_L(t) &= Ni(t) \int_l \left(d\vec{l} \times \vec{B}(t) \right) \\ &= Ni(t) \int_l B(t) dl \sin\theta\end{aligned}\quad (1)$$

where N is the number of turns of the coil, $i(t)$ is the coil current, l is the coil length, $B(t)$ is the magnetic flux density through the coil, and θ is the angle between the magnetic flux density and the current flow direction in the coil. Here, the maximum Lorentz force is generated when $\theta = 90^\circ$ or -90° for the same amplitudes of the other parameters in Equation (1). Because the proposed IMLA requires Z-direction force, it is structuralized as shown in Figure 3a.

3. Lorentz Force Prediction of the Proposed IMLA by a Magnetic Equivalent Circuit with a Magnetostatic Analysis

The Lorentz force determined by Equation (1) can be quickly predicted from the magnetic flux obtained by a MEC [24–26]. Therefore, for a magnetostatic analysis, a simple MEC analysis was conducted to elucidate the electromagnetic phenomenon and analyze the approximate Lorentz force of the proposed IMLA. For the MEC analysis, the following three assumptions are considered.

Assumption 1: The relative permeability of solid core is considered as a linear value of linear region of the solid core material.

Assumption 2: The relative permeability of the coil and bobbin housing is equal to air.

Assumption 3: The PM magnetization direction is along the X-direction.

The equivalent circuit model of the PM that can be expressed both as a flux source and as a magnetomotive force (MMF) source can be expressed as shown in Figure 4. For the MEC in this work, an MMF source is selected. The MMF of PM \mathcal{F}_m is defined as follows:

$$\mathcal{F}_m = \frac{B_r}{\mu_0 \mu_{rm}} h_m \quad (2)$$

where B_r is the PM residual flux density, μ_0 is the vacuum permeability, μ_{rm} is the PM relative permeability, and h_m is the PM height.

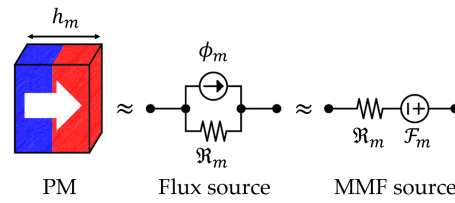


Figure 4. The equivalent circuit model of the PM.

The total MEC model of the proposed IMLA considering the leakage flux of the PM is illustrated in Figure 5, where $\mathfrak{R}_{c1} \sim \mathfrak{R}_{c12}$ are the reluctances of solid cores, $\mathfrak{R}_{air1} \sim \mathfrak{R}_{air4}$ are the reluctances of the air gap containing the bobbin housing and winding, $\mathfrak{R}_{pm1} \sim \mathfrak{R}_{pm4}$ are the reluctances of the PMs, $\mathcal{F}_{pm1} \sim \mathcal{F}_{pm4}$ are the MMF of the PMs, and $\mathcal{F}_{w1} \sim \mathcal{F}_{w2}$ are the MMF of the windings. The width of the coil is smaller than that of the PM, and leakage flux, which does not generate a Lorentz force because it does not cross the coil, exists at the edges of both sides of the PM. The total MEC model without PM leakage flux shows that there are five flux loops of $\phi_A \sim \phi_E$. Here, the practical flux that generates the Lorentz force in coils is $\phi_{m1} \sim \phi_{m4}$. However, the PM leakage flux is not usable. It is used as practical flux when the stroke is changed. This is why the width of the PM is greater than the width of the coil.

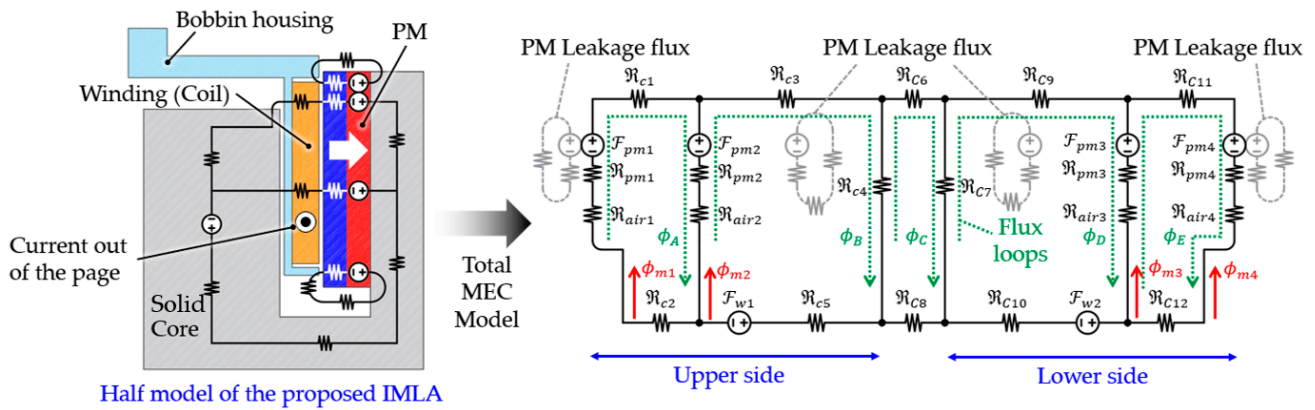


Figure 5. The MEC model of the proposed IMLA.

To obtain $\phi_{m1} \sim \phi_{m4}$, a mesh current analysis (loop current method) of the equivalent electric circuit is used since it is similar to the MEC. The reluctances for each section are calculated based on the shapes and are listed in Table 2. Here, μ is the absolute magnetic permeability of a material.

Table 2. Reluctance calculation of the MEC of the proposed IMLA.

Reluctances	Equation	Schematic
$\mathfrak{R}_{c4}, \mathfrak{R}_{c7},$ $\mathfrak{R}_{air1} \sim \mathfrak{R}_{air4},$ $\mathfrak{R}_{pm1} \sim \mathfrak{R}_{pm4}$	$\int_{r_A}^{r_B} \frac{1}{2\pi\mu r h} dr = \frac{1}{2\pi\mu h} \ln\left(\frac{r_B}{r_A}\right)$	
$\mathfrak{R}_{c1} \sim \mathfrak{R}_{c3},$ $\mathfrak{R}_{c5} \sim \mathfrak{R}_{c6},$ $\mathfrak{R}_{c8} \sim \mathfrak{R}_{c12}$	$\frac{h}{\pi\mu(r_B^2 - r_A^2)}$	

For the magnetostatic analysis, the maximum winding MMF when the current direction is out of the page where the moving direction is upwards is considered. The 5×5 matrix form for $\phi_A \sim \phi_E$ based on the mesh current analysis is expressed as follows:

$$\begin{bmatrix} \mathfrak{R}_A & \mathfrak{R}_B & 0 & 0 & 0 \\ \mathfrak{R}_B & \mathfrak{R}_C & \mathfrak{R}_D & 0 & 0 \\ 0 & \mathfrak{R}_D & \mathfrak{R}_E & \mathfrak{R}_F & 0 \\ 0 & 0 & \mathfrak{R}_F & \mathfrak{R}_G & \mathfrak{R}_H \\ 0 & 0 & 0 & \mathfrak{R}_H & \mathfrak{R}_I \end{bmatrix} \begin{bmatrix} \phi_A \\ \phi_B \\ \phi_C \\ \phi_D \\ \phi_E \end{bmatrix} = \begin{bmatrix} 0 \\ \mathcal{F}_{pm2} - \mathcal{F}_{w1} \\ 0 \\ -\mathcal{F}_{w2} - \mathcal{F}_{pm3} \\ 0 \end{bmatrix} \tag{3}$$

where $\mathfrak{R}_A \sim \mathfrak{R}_I$ are the total reluctances related to magnetic flux for each loop, as follows:

$$\begin{aligned} \mathfrak{R}_A &= \mathfrak{R}_{air1} + \mathfrak{R}_{pm1} + \mathfrak{R}_{c1} + \mathfrak{R}_{pm2} + \mathfrak{R}_{air2} + \mathfrak{R}_{c2} \\ \mathfrak{R}_B &= -(\mathfrak{R}_{pm2} + \mathfrak{R}_{air2}) \\ \mathfrak{R}_C &= \mathfrak{R}_{pm2} + \mathfrak{R}_{air2} + \mathfrak{R}_{c3} + \mathfrak{R}_{c4} + \mathfrak{R}_{c5} \\ \mathfrak{R}_D &= -\mathfrak{R}_{c4} \\ \mathfrak{R}_E &= \mathfrak{R}_{c4} + \mathfrak{R}_{c6} + \mathfrak{R}_{c7} + \mathfrak{R}_{c8} \\ \mathfrak{R}_F &= -\mathfrak{R}_{c7} \\ \mathfrak{R}_G &= \mathfrak{R}_{c7} + \mathfrak{R}_{c9} + \mathfrak{R}_{pm3} + \mathfrak{R}_{air3} + \mathfrak{R}_{c10} \\ \mathfrak{R}_H &= -(\mathfrak{R}_{pm3} + \mathfrak{R}_{air3}) \\ \mathfrak{R}_I &= \mathfrak{R}_{air3} + \mathfrak{R}_{pm3} + \mathfrak{R}_{c11} + \mathfrak{R}_{pm4} + \mathfrak{R}_{air4} + \mathfrak{R}_{c12} \end{aligned} \tag{4}$$

The calculated $\phi_A \sim \phi_E$ by inverse matrix calculation of Equation (4) are presented as follows:

$$\begin{bmatrix} \phi_A \\ \phi_B \\ \phi_C \\ \phi_D \\ \phi_E \end{bmatrix} = \begin{bmatrix} 0.129 \\ 2.127 \\ 0.198 \\ -2.734 \\ -0.166 \end{bmatrix} \text{ (mWb)} \tag{5}$$

Finally, $\phi_{m1} \sim \phi_{m4}$ in Figure 5 can be obtained by the given values of the following Equation (5):

$$\begin{bmatrix} \phi_{m1} \\ \phi_{m2} \\ \phi_{m3} \\ \phi_{m4} \end{bmatrix} = \begin{bmatrix} \phi_A \\ \phi_B - \phi_A \\ \phi_E - \phi_D \\ -\phi_E \end{bmatrix} = \begin{bmatrix} 0.129 \\ 1.998 \\ 2.568 \\ 0.166 \end{bmatrix} \text{ (mWb)} \tag{6}$$

It should be noted that the magnetic flux value of each side is different because the winding MMF of the upper side reduces the PM MMF of the upper side, whereas the winding MMF of the lower side is added with the lower side PM MMF when the current direction is out of the page. The calculated main parameters by Equation (6) are presented in Table 3. Since the magnetic flux for each side is different, the Lorentz forces are also different. If the current direction is into the page, the Lorentz force of the upper side is greater than that of the lower side.

Table 3. Comparison of the Lorentz force between MEC and FEM.

	Lorentz Force (N)		
	Upper Side	Lower Side	Total
MEC	64.7	83.2	147.9
FEM	68.4	77.1	145.5

Figure 6 shows the Lorentz force with different strokes in magnetostatic FEM analysis. This analysis should be conducted because it is important to keep a constant force according to the strokes' change. Without considering the eddy current, the Lorentz force and the inertia force of the movers are almost the same. The change in the Lorentz force and the

inertial force of the movers within the change in the stroke was found to be about 5N. Flux density distribution shows that the flux density distribution of the lower solid core part is a little higher than that of the upper solid core part due to the added magnetic flux of the winding MMF and PM of the lower part.

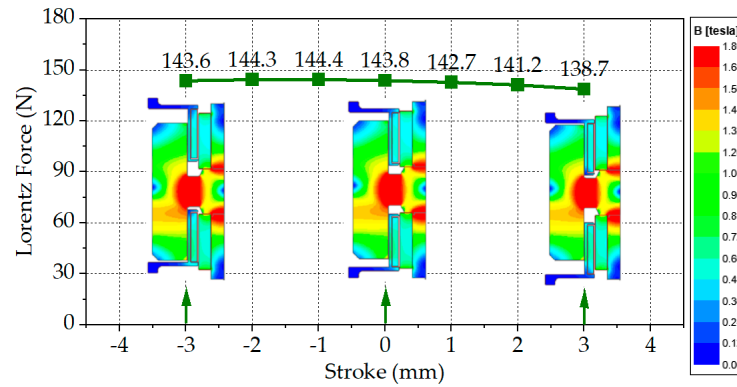


Figure 6. The Lorentz force (FEM) of the proposed IMLA with different strokes.

4. Dynamic Analysis Considering Co-Simulation of the Proposed IMLA

In dynamic motion, the required load force is above 120 N at three times the operating frequency of the natural frequency of the proposed IMLA. A dynamic characteristics analysis of the proposed IMLA, which was designed by the MEC, was conducted by co-simulation with FEM model and the electric circuit, as shown in Figure 3. The Lorentz force with the equation of linear motion is expressed as follows:

$$\vec{F}_L(t) = m\ddot{x}(t) + c\dot{x}(t) + kx(t) \tag{7}$$

where m , c , and k are the mass, damping, and stiffness coefficient of the structure, respectively, and \ddot{x} , \dot{x} , and x are the acceleration, velocity, and displacement, respectively. Here, $m\ddot{x}(t)$ is the inertial mass force, which is equal to the load force. Therefore, the inertial force can be expressed as follows:

$$m\ddot{x}(t) = \vec{F}_L(t) - c\dot{x}(t) - kx(t) \tag{8}$$

The Lorentz force $\vec{F}_L(t)$ is generated in the coil; it is then transmitted to the moving part. However, it should be noted that the term $c\dot{x}(t)$ is generated by the eddy current effect in the PMs, solid cores, and bobbin housing, and its force can be expressed as follows [27,28]:

$$F_c = \sigma\dot{x}B^2V = c_eV \tag{9}$$

where σ is the electrical conductivity of the material and V is the volume. The term c_e can be considered as the damping coefficient of the eddy current.

Figure 7 shows various results that are obtained according to the consideration of the eddy current loss according to the material characteristics of key components through a coupled analysis at $3f_n$. Since the bobbin housing supporting the coil winding, as shown in Figure 3, is aluminum, which has a high electrical conductivity, it is confirmed that the Lorentz force generated in the coil decreases by 23%. Applying materials with relatively low electrical conductivity can reduce the eddy current loss, thereby improving the efficiency of transmitting Lorentz forces generated from coils to inertial masses. However, an appropriate trade-off between the electrical conductivity and the strength of the material is required.

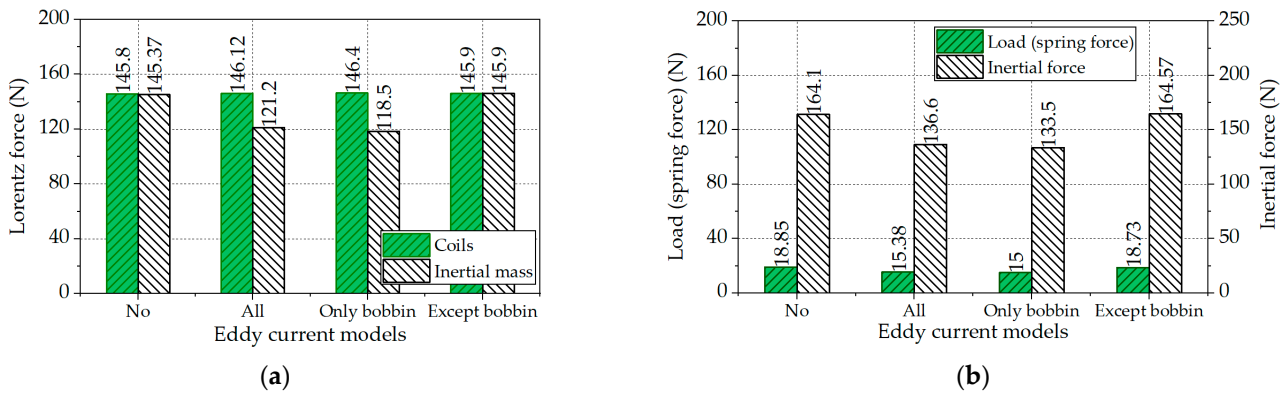


Figure 7. Forces comparison of the proposed IMLA at $3f_n$. (a) Lorentz forces of coils and inertia mass; (b) load and inertial forces.

Figure 8 shows the transient dynamic analysis results of the main variables. Because current from voltage source is applied, there is an initial transient response until 60 ms. Figure 8a shows the results of various forces, such as the Lorentz force in the coils, the inertial mass force in the PM and solid core, the load force in springs, and the transmitted force as the inertial mass force, considering the loss of eddy current of key components through a coupled analysis at $3f_n$. Because the Lorentz force is the action force, the other forces are the reaction forces, and, thus, there is 180° anti-phase between the action force and the reaction forces. The load force is obtained by multiplying the generated vibration displacement by the spring coefficient, and, thus, it can be confirmed that the tendency of vibration displacement is the same. When the force transferred to the inertial mass is added to the spring force, it becomes the inertial mass force. Figure 8b shows the results of the induced voltage and current. These show that the induced voltage and current of both coil parts are balanced waveforms according to time. The value of the peak current is 3 A, which is within the limited range of the required design.

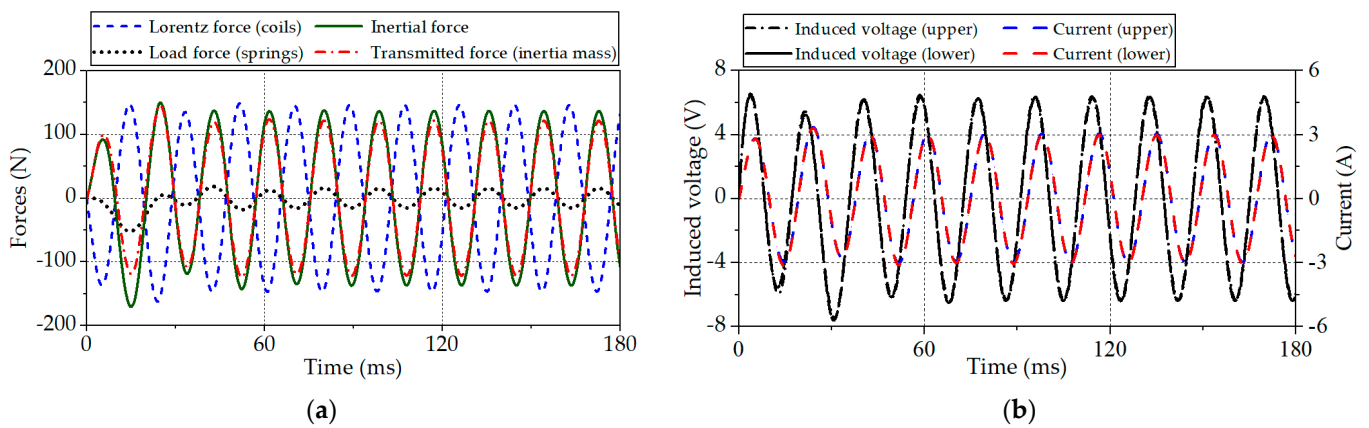


Figure 8. Transient dynamic analysis results of the proposed IMLA at $3f_n$. (a) Lorentz, load, and inertial mass forces comparison; (b) induced voltages and currents of the upper and lower coils.

Figure 9a presents the vibration displacement of the inertial mass (PM + solid core), which was determined to be $0.776 \text{ mm}_{\text{peak-peak}}$ from the analysis. The eddy current loss of the PM and bobbin housing was determined to be $14.64 \text{ W}_{\text{rms}}$. Figure 9b shows the inductance and the flux linkage in the upper and lower winding, which were determined to be $17.4 \text{ mH}_{\text{rms}}$ and $0.288 \text{ Wb}_{\text{rms}}$, respectively.

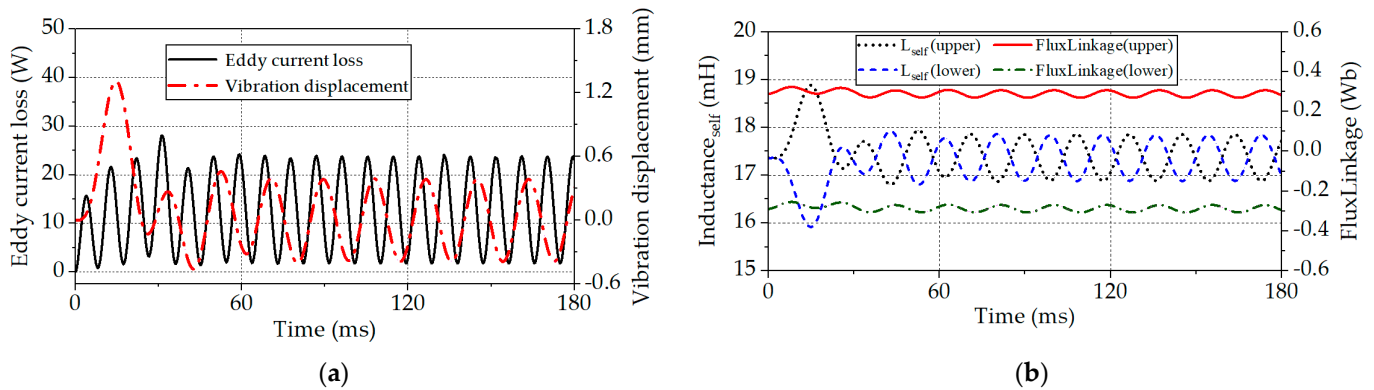


Figure 9. Transient dynamic analysis results of the proposed IMLA at $3f_n$. (a) Eddy current loss and vibration displacement; (b) inductance and flux linkage of the upper and lower coils.

Figure 10a shows a comparison of the inertial and damping forces according to the eddy current loss of the material used when the current peak is 3A. In general, eddy current loss occurs when magnetic flux passes through a material with a high electrical conductivity. The Lorentz force generated by the coil reduces the force transmitted to the inertial mass because of the eddy current loss of the bobbin housing (aluminum) supporting the coil. The reduced force transmitted to the inertial mass is the damping force and is evaluated to have a peak of about 47 N.

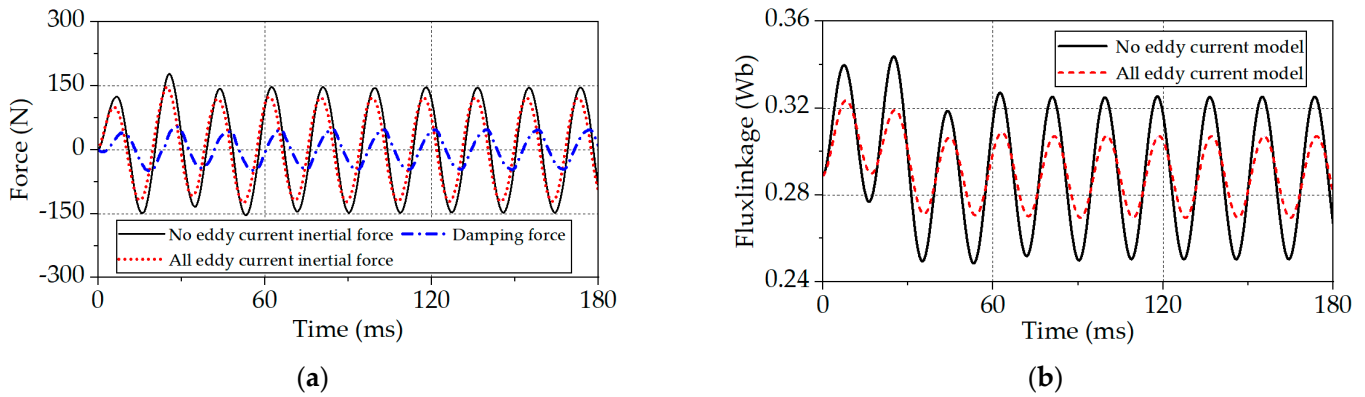


Figure 10. Transient dynamic analysis results of the proposed IMLA at $3f_n$. (a) Comparison of damping force and inertial force; (b) flux linkage of a half coil according to the eddy current of the material.

Figure 10b presents a comparison of the flux linkage of a half coil according to the eddy current loss of the material used when the current peak is 3A. The material (aluminum) of the bobbin housing that supports the coil causes an eddy current, which prevents the magnetic flux from passing through the coil. Therefore, it is shown that the flux linkage is reduced.

All constraints must be satisfied in this work. It was confirmed that the constraints of the phase difference between the force and the current, the phase difference from the magnitude to the operating force at $3f_n$, the frequency operating range, the linearity of the force, the dynamic range, and the harmonic distortion were all satisfied. In Section 3, a difference in force between the upper and lower coils is presented in Table 3. However, there is no unbalance effect for each coil’s induced voltage, current, and flux linkage when operating the proposed IMLA in dynamic operation, as shown in Figures 8b and 9b.

Figure 11 shows the flux line, Lorentz force on edge of the bobbin housings and coils, flux density vector, and flux density distribution at the proposed IMLA model at $3f_n$. Leakage flux lines, as shown in Figure 11a, are investigated. When the inertial mass part is

moved, leakage flux is utilized as linkage flux through the coils, which generate upper and lower direction Lorentz forces.

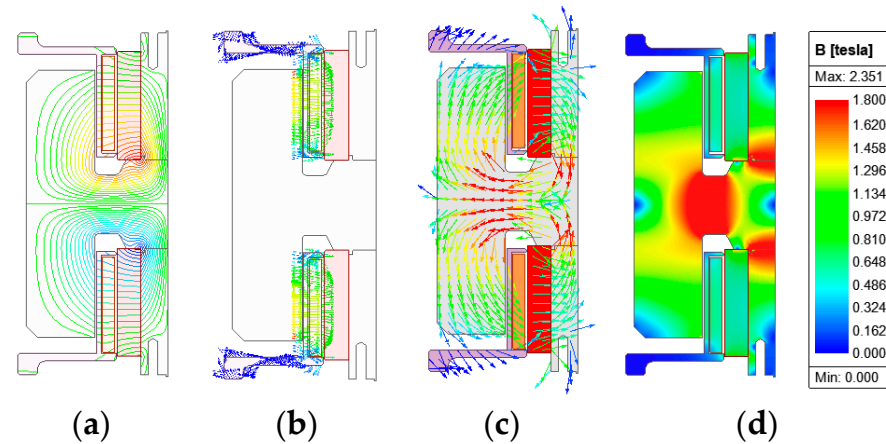


Figure 11. Electromagnetic distribution of the proposed IMLA. (a) Flux lines, (b) Lorentz force vector on edge of the bobbing housings and coils, (c) flux density vector, and (d) flux density distribution at $3f_n$.

Improving thrust force is possible not only from an optimization standpoint but also from material selection. Figure 12 shows the B–H nonlinear curve according to the three materials (S20C, S45C, and SPCC) of carbon steel. In the linear region of the B–H nonlinear curve, when a material with a high permeability is effective and a material has a high saturation magnetic flux density, the thrust force of the linear actuator applied with S20C material is improved by more than 10%.

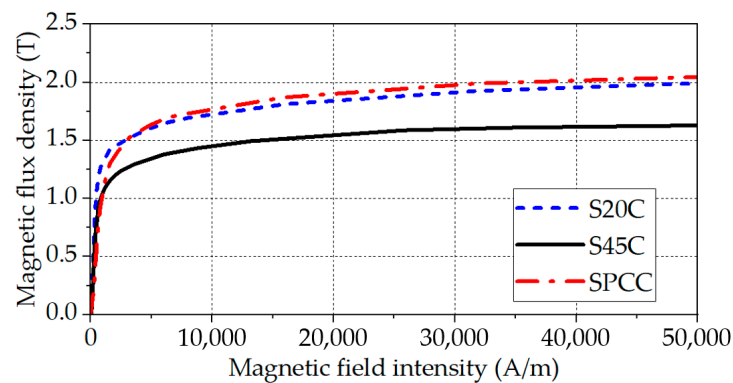


Figure 12. B–H curve comparison of solid core materials.

Figure 13 shows a comparison of various forces and vibration displacement according to the solid core material of the proposed IMLA model at $3f_n$. The thrust force performance of the S20C material was improved by more than 10% compared to the S45C material, as shown in Figure 13a. It has been confirmed that S20C and SPCC materials have almost the same performance. When a high thrust is required within such a limited volume, it is necessary to select and apply a solid core material with a high permeability and saturation magnetic flux density. As forces increase, the vibration displacement also increases, as shown in Figure 13b.

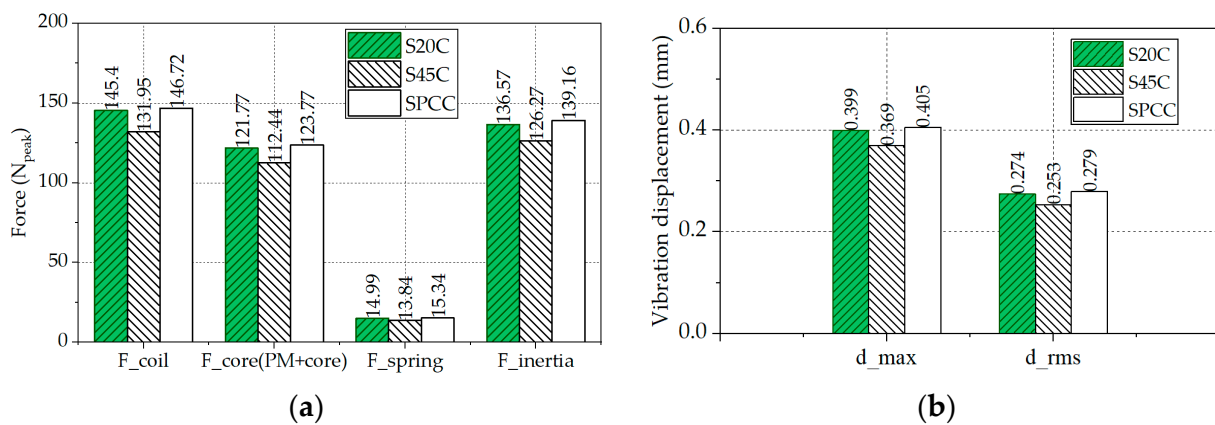


Figure 13. Forces comparison with different materials of the proposed IMLA at $3f_n$. (a) Forces in the coil, solid core with PM, spring, and inertia; (b) vibration displacement according to the solid core material.

5. Conclusions

In this work, we present an inertial mass linear actuator (IMLA) based on Lorentz forces for active vibration control systems in large ships. For theoretical understanding based on electromagnetic phenomena, magnetic equivalent circuit (MEC) analysis was performed for magnetic static analysis with linear regions. The calculated Lorentz force is almost identical to the finite element method (FEM), but within an acceptable range. The differences in calculated force between MEC and FEM are generated because MEC analysis considers a linear relative permeability of solid core, namely the lumped parts of the IMLA. However, it is important to the understand electromagnetic phenomenon of the proposed IMLA.

The operation of precision control requires an operating force of at least 120 N at an operating frequency three times higher than the actuator's natural frequency. Through the coupled analysis of an electrical circuit and finite element analysis, the actual situation of the AC source was simulated without assuming current and inductance. As a result of dynamic analysis, it was confirmed that the damping force due to eddy current loss in the bobbin housing of the coil was significant. It was found that the Lorentz force generated by the coil reduced the force transmitted by inertial force to the damping force due to an eddy current in the bobbin housing. The model was confirmed through various performance analyses according to the required specifications. In future studies, we would like to further validate the analysis results through experimental verification of the proposed IMLA.

Author Contributions: Conceptualization, D.-K.H.; methodology, D.-K.H.; software, D.-K.H.; validation, D.-K.H. and J.-H.P.; formal analysis, J.-H.P.; investigation, J.-H.P.; resources, D.-K.H.; data curation, D.-K.H.; writing—original draft preparation, D.-K.H. and J.-H.P.; writing—review and editing, D.-K.H. and J.-H.P.; visualization, J.-H.P.; supervision, D.-K.H.; project administration, D.-K.H.; funding acquisition, D.-K.H. All authors have read and agreed to the published version of the manuscript.

Funding: This work was supported by an Agency for Defense Development Grant funded by the Korean government (UC210001DD).

Data Availability Statement: Some or all of the data and the models generated or used during the study are available in a repository or online.

Conflicts of Interest: The authors declare no conflict of interest.

References

1. Halliday, W.D.; Pine, M.K.; Citta, J.J.; Harwood, L.; Hauser, D.D.W.; Hilliard, R.C.; Lea, E.V.; Loseto, L.L.; Quakenbush, L.; Insley, S.J. Potential Exposure of Beluga and Bowhead Whales to Underwater Noise from Ship Traffic in the Beaufort and Chukchi Seas. *Ocean Coast. Manag.* **2021**, *204*, 105473. [[CrossRef](#)]
2. Williams, R.; Wright, A.J.; Ashe, E.; Blight, L.K.; Bruintjes, R.; Canessa, R.; Clark, C.W.; Cullis-Suzuki, S.; Dakin, D.T.; Erbe, C.; et al. Impacts of Anthropogenic Noise on Marine Life: Publication Patterns, New Discoveries, and Future Directions in Research and Management. *Ocean Coast. Manag.* **2015**, *115*, 17–24. [[CrossRef](#)]
3. Spence, J.H.; Fischer, R.W. Requirements for Reducing Underwater Noise from Ships. *IEEE J. Ocean. Eng.* **2017**, *42*, 388–398. [[CrossRef](#)]
4. Kudźma, Z.; Stosiak, M. Reduction of Infrasonics in Machines with Hydrostatic Drive. *Acta Bioeng. Biomech.* **2013**, *15*, 51–64.
5. Howard, C. *Recent Developments in Submarine Vibration Isolation and Noise Control*; Engineers: Spring Hill, Australia, 2011.
6. Karpenko, M.; Skačkauskas, P.; Prentkovskis, O. Methodology for the Composite Tire Numerical Simulation Based on the Frequency Response Analysis. *Ekspluat. Niezawodn.–Maint. Reliab.* **2023**, *25*. [[CrossRef](#)]
7. Winberg, M.; Hansen, C.; Claesson, I.; Li, X. Active Control of Engine Vibrations in a Collins Class Submarine. Blekinge Institute of Technology Research Report. 2003. Available online: <http://urn.kb.se/resolve?urn=urn:nbn:se:bth-00239> (accessed on 3 July 2023).
8. Broomhead, T.; Manzie, C.; Hield, P.; Brear, M. An Experimental Investigation of Additional Actuators on a Submarine Diesel Generator. *Control Eng. Pract.* **2016**, *55*, 26–37. [[CrossRef](#)]
9. Lee, B.-H.; Lee, C.-W. Model Based Feed-Forward Control of Electromagnetic Type Active Control Engine-Mount System. *J. Sound Vib.* **2009**, *323*, 574–593. [[CrossRef](#)]
10. Daley, S.; Johnson, F.A.; Pearson, J.B.; Dixon, R. Active Vibration Control for Marine Applications. *Control Eng. Pract.* **2004**, *12*, 465–474. [[CrossRef](#)]
11. Caresta, M.; Kessissoglou, N. Active Control of Sound Radiated by a Submarine Hull in Axisymmetric Vibration Using Inertial Actuators. *J. Vib. Acoust.* **2012**, *134*, 011002. [[CrossRef](#)]
12. Li, Y.; He, L.; Shuai, C.-G.; Wang, C.-Y. Improved Hybrid Isolator with Maglev Actuator Integrated in Air Spring for Active-Passive Isolation of Ship Machinery Vibration. *J. Sound Vib.* **2017**, *407*, 226–239. [[CrossRef](#)]
13. Yang, T.; Wu, L.; Li, X.; Zhu, M.; Brennan, M.J.; Liu, Z. Active Vibration Isolation of a Diesel Generator in a Small Marine Vessel: An Experimental Study. *Appl. Sci.* **2020**, *10*, 3025. [[CrossRef](#)]
14. Phu, D.X.; Choi, S.B.; Lee, Y.S.; Han, M.S. Design of a New Engine Mount for Vertical and Horizontal Vibration Control Using Magnetorheological Fluid. *Smart Mater. Struct.* **2014**, *23*, 117001. [[CrossRef](#)]
15. Moon, S.-J.; Kwak, J.-S.; Chung, J.-H.; Ji, Y.-J.; Yoon, J.-S.; Choi, S.-B.; Lee, H.-Y.; Jung, W.-J.; Ki, D.-J. A Study on the Hybrid Mount against Vibration and Shock for Naval Ships. *Shock Vib.* **2010**, *17*, 269–283. [[CrossRef](#)]
16. Choi, S.-B.; Sohn, J.W.; Choi, S.-M.; Nguyen, V.Q.; Moon, S.-J. A Piezostack-Based Active Mount for Broadband Frequency Vibration Control: Experimental Validation. *Smart Mater. Struct.* **2009**, *18*, 097001. [[CrossRef](#)]
17. Huber, J.E.; Fleck, N.A.; Ashby, M.F. The Selection of Mechanical Actuators Based on Performance Indices. *Proc. Math. Phys. Eng. Sci.* **1997**, *453*, 2185–2205. [[CrossRef](#)]
18. Aabid, A.; Hrairi, M.; Mohamed Ali, S.J.; Ibrahim, Y.E. Review of Piezoelectric Actuator Applications in Damaged Structures: Challenges and Opportunities. *ACS Omega* **2023**, *8*, 2844–2860. [[CrossRef](#)]
19. Luo, C.; Zhao, R. Analysis and Restraining of Eddy Current Damping Effect in Linear Voice Coil Motor. *IET Electr. Power Appl.* **2020**, *14*, 837–842. [[CrossRef](#)]
20. Liu, Y.; Zhang, M.; Zhu, Y.; Yang, J.; Chen, B. Optimization of Voice Coil Motor to Enhance Dynamic Response Based on an Improved Magnetic Equivalent Circuit Model. *IEEE Trans. Magn.* **2011**, *47*, 2247–2251. [[CrossRef](#)]
21. Kim, J.-Y.; Ahn, D. Analysis of High Force Voice Coil Motors for Magnetic Levitation. *Actuators* **2020**, *9*, 133. [[CrossRef](#)]
22. Herold, S.; Mayer, D. Adaptive Piezoelectric Absorber for Active Vibration Control. *Actuators* **2016**, *5*, 7. [[CrossRef](#)]
23. Winberg, M.; Johansson, S.; Claesson, I. Inertial Mass Actuators, Understanding and Tuning. In Proceedings of the 11th International Congress on Sound and Vibration (ICSV11), St. Petersburg, Russia, 5–8 July 2004; The International Institute of Acoustics and Vibration (IIAV): Gliwice, Poland, 2004.
24. Loussert, G.; Alzingre, J.-D. A Magnetic and Mechanical Force Model for the Design of an Archimedean Spiral Flexure Bearing for a Linear Direct-Drive Electromagnetic Actuator. *IEEE ASME Trans. Mechatron.* **2019**, *24*, 1617–1627. [[CrossRef](#)]
25. Batdorff, M.A.; Lumkes, J.H. High-Fidelity Magnetic Equivalent Circuit Model for an Axisymmetric Electromagnetic Actuator. *IEEE Trans. Magn.* **2009**, *45*, 3064–3072. [[CrossRef](#)]
26. Meng, B.; Xu, H.; Liu, B.; Dai, M.; Zhu, C.; Li, S. Novel Magnetic Circuit Topology of Linear Force Motor for High Energy Utilization of Permanent Magnet: Analytical Modelling and Experiment. *Actuators* **2021**, *10*, 32. [[CrossRef](#)]

27. Abdullah; Ahn, J.-H.; Kim, H.-Y. Effect of Electromagnetic Damping on System Performance of Voice-Coil Actuator Applied to Balancing-Type Scale. *Actuators* **2020**, *9*, 8. [[CrossRef](#)]
28. Sodano, H.A.; Inman, D.J. Non-Contact Vibration Control System Employing an Active Eddy Current Damper. *J. Sound Vib.* **2007**, *305*, 596–613. [[CrossRef](#)]

Disclaimer/Publisher’s Note: The statements, opinions and data contained in all publications are solely those of the individual author(s) and contributor(s) and not of MDPI and/or the editor(s). MDPI and/or the editor(s) disclaim responsibility for any injury to people or property resulting from any ideas, methods, instructions or products referred to in the content.